Simulation of char-pellet combustion and sodium release inside porous char using lattice Boltzmann method

Yingzu Liu [a,b], Jun Xia [b,*], Kaidi Wan [a], Luc Vervisch [c], Zhihua Wang [a,*], Hua Zhao [b], Kefa Cen [a]

[a] State Key Laboratory of Clean Energy Utilization, Zhejiang University, 310027, Hangzhou, PR China
[b] Department of Mechanical and Aerospace Engineering & Institute of Energy Futures, Brunel University London, Uxbridge UB8 3PH, UK
[c] CORIA – CNRS, Normandie Université, INSA de Rouen, 76800 Saint-Etienne-du-Rouvray, France

ABSTRACT

Char-pellet combustion is studied with the lattice Boltzmann method (LBM) including sodium release and the ash inhibition effect on oxygen diffusion in the porous char. The sodium release and the shrinking of the char pellet are simulated by accounting for the reactions occurring both in the solid and gas phases. The combustion of a single char pellet is considered first, and the results are compared against measurements. The simulation of the pellet mass, pellet temperature and sodium release agreed well with in-house optical measurements. The validated lattice Boltzmann approach is then extended to investigate the combustion of porous char and sodium release inside the porous medium. The pore-structure evolution and the flow path variation are simulated as combustion proceeds. The simulations reproduce the expected different behaviors between the combustion products (CO and CO_2) and the released volatile, here the sodium vapor. The combustion products are mostly generated at the flame front and then transported by the flow and molecular diffusion inside the complex porous char structure. However, the volatile sodium vapor forms in the entire porous char and tends to accumulate in regions where the flow motion stays weak, as in internal flow microchannels, or blocked, as in closed pores. These results confirm the potential of the LBM formalism to tackle char-pellet combustion accounting for the topology of the porous medium.

© 2019 The Author(s). Published by Elsevier Inc. on behalf of The Combustion Institute.
This is an open access article under the CC BY license. (http://creativecommons.org/licenses/by/4.0/)

1. Introduction

In computational fluid dynamics (CFD), the flow evolution is usually described by Navier–Stokes (NS) equations, from the macro scale (e.g., jet engines and furnaces) down to the micro scale (e.g., electric chips and batteries). Over the past three decades, a simulation method based on the mesoscopic fluid dynamics, the lattice Boltzmann method (LBM), has attracted great interest and attention in the CFD community. Unlike traditional methods, the LBM does not deal with the discretized NS equations, but models flow dynamics by using the discrete Boltzmann equation and through the evolution of the distribution functions [1,2]. There are several advantages of the LBM as compared to traditional CFD methods [3]: (1) the scheme is simple. The LBM simulates flow with linear equations with relaxation processes; (2) it is easy to deal with complex geometry by changing only the form of distribution func-

tions in the simulation; (3) it is convenient for parallel coding and computing. The advantages of the LBM made this approach widely applied to a variety of flow research areas such as: (1) multiphase and multispecies flow [4,5]; (2) microchannel flow and heat transfer [6,7]; (3) nanofluid [8,9] and (4) porous medium flow [10,11].

The oxidization of porous coal/biomass/char at high temperature is a fundamental process of solid fuel combustion. However, the porous char features a very complex geometry, embedding flow microchannels and micropores [12], and it is challenging for traditional Navier-Stokes based methods to simulate the reaction of char in such a complex geometry. On the other hand, due to its capability of dealing with complex geometry, early applications of the Lattice Boltzmann method have focused on flow dynamics in porous medium, e.g., flow seeping and wetting of the porous structure [3]. Buckle et al. [13] simulated the permeability of flow in a sandstone based on the X-ray image of the porous sandstone structure. Their LBM simulation results agreed well with experimental ones. Based on what was observed in the simulation, they improved the model of flow penetration in a porous structure. In recent years, the LBM has been upgraded for simulating more

* Corresponding authors.
E-mail addresses: jun.xia@brunel.ac.uk (J. Xia), wangzh@zju.edu.cn (Z. Wang).

Nomenclature

LBM approach

f	the distribution function for density
g	the distribution function for scalars
f^{eq}	the equilibrium distribution function for density
g^{eq}	the equilibrium distribution function for density
ρ	gas phase density in LBM
G	scalars: temperature and species mass fractions
ω	weight factor for the different speed vectors
τ	the relaxation time
c	rescaled thermal velocity
u	the macroscopic velocity
e	the base velocity in LBM
ν	the kinematic viscosity in LBM
κ	the diffusion coefficient in LBM
Pr	Prandtl number
Sc	Schmidt number
Re	Reynolds number
t	time in LBM
δ_t	time step in LBM
dt	the LBM time step in physical units (s)
F	the external force for flow velocity in LBM
Q	the source term for scalars in LBM
R	the universal gas constant

Char combustion model

X	species mole fraction
Y	species mass fraction
T	gas-phase temperature (K)
N_p	the CO/CO$_2$ mole ratio
A_s	the reaction surface area (m^2)
i	the vector of the discrete molecular velocities
$C_{o,surface}$	the oxygen mass per unit area on the particle surface (kg/m^2)
m_{comb}	the char combustion rate (kg/s)
k_D	the oxygen diffusion coefficient (m^2/s)
T_{char}	the solid-phase temperature (K)
δ	the ash thickness (m)
Sh	the Sherwood number
θ	the porosity of ash
d_p	the pellet diameter (m)
d_c	the char core pellet diameter (m)
C_{char}	the carbon conversion ratio
m_{ash}	the mass of ash (kg)
m_c	the mass of char core (kg)
ρ_{ash}	the ash density (kg/m^3)
ρ_c	the char density (kg/m^3)
m_p	the pellet mass (kg)
C_{Na}	the sodium mass fraction in the char
Na_{flux}	the sodium release rate (kg/s)
k	the CO$_2$ production rate (kg/s)
Q_{rad}	the thermal radiation heat source (kJ/s)
Q_{comb}	the char combustion released heat (kJ/s)
m_{s_comb}	the mass consumption of the solid phase (kg)
Δ	the grid resolution of the LBM (m)
ε	the char surface emissivity
σ	the Stefan–Boltzmann constant (W/(m^2 K^4))
C_p	the heat capacity (kJ/(kg K))
f_{phase}	the phase function
f_{gs}	the mask to indicate whether the local grid point is in the gas (0) or solid (1) phase
N_{gas}	grid number of the gas phase

Subscripts

0	initial status

complex flow and transport phenomena in porous medium. Kang et al. [14] employed the LBM in the simulation of crystal and colony growth. Chen et al. [15] investigated dissolution and precipitation of solid in a solution and analyzed the effect of precipitation on the surface reaction. Gao et al. [16] employed the LBM to simulate acid treatment on mineral in coal, and compared different reactions of minerals and the effect of acid treatment on the coal structure.

Research on the application of the LBM approach to combustion has also been developed over the past two decades. Yamamoto et al. [17] simulated propane combustion in Ni-Cr porous medium and observed asymmetric burning inside the porous medium. The higher temperature than the metal's melting point may then destroy the solid structure. Recently Lin and Luo [18] employed the Boltzmann model to investigate hydrodynamic and thermo-dynamic nonequilibrium effects around a detonation wave and the effects of different relaxation times on the chemical reactants, products and the relative height of the detonation peak were obtained. Boivin et al. [19] presented a variable-density LBM solver, which successfully simulated a classical freely propagating flame as well as a counterflow diffusion flame, with strains up to extinction. To numerically solve premixed, nonpremixed, or partially premixed nonequilibrium multi-component reactive flows, a discrete Boltzmann model (DBM) has been developed by Lin et al. [20], which presents not only more accurate hydrodynamic quantities, but also detailed nonequilibrium effects that are essential yet long-neglected by traditional fluid dynamics. Furthermore, a multiple-relaxation-time discrete Boltzmann model was developed for compressible thermal reactive flow [21]. Via the Chapman–Enskog analysis, the developed multiple-relaxation-time DBM is demonstrated to recover reactive Navier–Stokes (NS) equations in the hydrodynamic limit. Improvement of overall mass conservation in LBM simulation of multicomponent combustion problems has been achieved in [22]. Even though there have been considerable developments in the LBM community on solving multiphysics flow phenomena, including porous medium flow, premixed, non-premixed combustion and detonation cases, according to the best of our knowledge, LBM simulation of gas-solid two-phase porous-char combustion at the pore scale has not been attempted yet and is one objective of the present work.

During the combustion of sodium-rich coal or potassium-rich biomass, vapor of alkali metal (sodium and potassium) minerals are released under heating. The released alkali can condense on boiler walls, causing fouling and corrosion [23,24]. For instance, the sodium vapor (NaCl or Na$_2$CO$_3$) is easy to condense on heat exchanger surfaces and causes serious corrosion. Many researches have focused on the characteristics of alkali release using on-line and offline measurements [23]. An offline method samples the fuel and emission in different combustion stages and analyzes the sample using a chemical method, such as inductively coupled plasma-atomic emission spectrometry (ICP-AES) and X-ray diffraction (XRD). An online method employs optical instruments to measure time-resolved concentrations of gaseous species released from the burning solid-fuel, such as laser-induced breakdown spectroscopy (LIBS) [25,26], and planar laser induced fluorescence (PLIF) [27,28]. In our previous work, alkali release from a burning coal pellet was investigated using optical methods [25,27]. The alkali release, pellet mass and pellet temperature were simultaneously measured. The results show that alkali release can be divided into three stages, including the devolatilization, char burnout and ash stages, and most sodium is released during the char burnout

stage. Based on those experimental results, a preliminary kinetics of sodium release during coal-pellet burning was developed.

The authors have also performed high-fidelity simulation of laboratory-scale pulverized-coal flames to investigate sodium emissions in these turbulent gas-solid two-phase flames [29,30]. In [29], a subset of a detailed sodium chemistry [31] was tabulated and coupled with a large-eddy simulation solver to predict sodium emissions in a spatially developing pulverized-coal flame. In [30], direct numerical simulation (DNS) of a temporally developing pulverized-coal flame was performed. The predictions of sodium emissions were compared between tabulation based on one-dimensional premixed flamelets and DNS results. In these turbulent two-phase reacting flow simulations, pulverized-coal particles were approximated by point particles with mass, but no volume. Since there were no reliable data sources available on species compositions of the sodium compounds vapor released from a pulverized-coal particle under heating, it was also assumed in [29] and [30] that atomic sodium was released together with coal volatile during coal-particle pyrolysis. This constitutes a major assumption, which remains to be relaxed to improve predictions of sodium emissions in pulverized-coal combustion in future numerical studies. Along these lines, this study constitutes a first step to examine how alkali metal compounds are released from inside a burning porous coal/char particle, which is the second objective of this work.

In the present study, models for the solid-phase char combustion and sodium release are developed and implemented into the open-source LBM flow solver DL_MESO [32]. We first validate the LBM approach against our in-house experimental data of the combustion of a single 4-mm pellet [25]. In these experiments, the temperature varies by only 10% between 1600 K and 1760 K. As a first step, therefore, the simulations are performed assuming a constant gas density, which means the impact of temperature variation on the flow field is neglected, i.e., one-way coupling. Then, the validated numerical tool is used to simulate the combustion of a porous char particle in microscale, to explore char oxidation, sodium release, and their intricate connections.

2. Lattice Boltzmann method

A basic LBM approach is applied [33] with the Bhatnagar–Gross–Krook (BGK) approximation [3] to close the discretized Boltzmann equation. LBMs have been under rapid development to simulate high-Reynolds-number thermal and reactive flow with considerable temperature variation, e.g., by Luo and his co-workers on the cascaded LBM [34,35], multiple-relaxation-time LBMs [36], and discrete Boltzmann models [18,20]. In the present study where the Reynolds number is low and the temperature variation of the system is limited to 10%, the BGK model has been used and found to be able to properly predict our in-house experimental data of the combustion of a single coal pellet. The BGK method is based on the development of discrete molecular velocity distribution functions on uniform Cartesian lattices. The velocity distribution functions evolution is discretized as

$$f_i(\mathbf{x} + \mathbf{e}_i\delta_t, t + \delta_t) - f(\mathbf{x}, t) = -\frac{1}{\tau}\Big[f_i(\mathbf{x}, t) - f_i^{eq}(\mathbf{x}, t)\Big] + \omega_i F \quad (1)$$

$$f_i^{eq} = \omega_i\left\{f + f_0\left[3\frac{(\mathbf{e}_i \cdot \mathbf{u})}{c^2} + \frac{9}{2}\frac{(\mathbf{e}_i \cdot \mathbf{u})^2}{c^4} - \frac{3}{2}\frac{u^2}{c^2}\right]\right\} \quad (2)$$

$$\rho = \sum_i f_i \quad \rho\mathbf{u} = \sum_i f_i\mathbf{e}_i \quad \nu = \frac{2\tau - 1}{6}c^2\delta_t \quad (3)$$

Similarly, the governing equation for scalar distribution functions can be written as:

$$g_i(\mathbf{x} + \mathbf{e}_i\delta_t, t + \delta_t) - g(\mathbf{x}, t) = -\frac{1}{\tau}\Big[g_i(\mathbf{x}, t) - g_i^{eq}(\mathbf{x}, t)\Big] + \omega_i Q \quad (4)$$

$$g_i^{eq} = \omega_i\left\{g + g_0 \times 3\frac{(\mathbf{e}_i \cdot \mathbf{u})}{c^2}\right\} \quad (5)$$

$$G = \sum_i g_i \quad \kappa = \frac{2\tau - 1}{6}c^2\delta_t \quad (6)$$

f and g are the distribution function for density ρ and scalars G (temperature T and mass fractions Y of transported species, including O_2, CO, CO_2 and Na), respectively; the index i defines the vector of the discrete molecular velocities; ω_i is the weight factor for the different speed vectors; τ is the relaxation time; c is the rescaled thermal velocity; u is the macroscopic velocity; e is the base velocity in the LBM; ν and κ are the kinematic viscosity and diffusion coefficient in the LBM, respectively; F and Q are the external force for flow velocity and the source term for scalars, respectively. The relationship between the relaxation times and diffusion properties is expressed by the Prandtl number Pr and the Schmidt number Sc as:

$$\text{Pr} = \frac{\kappa_T}{\nu} = \frac{2\times\tau_\nu - 1}{2\times\tau_T - 1} \quad (7)$$

$$\text{Sc} = \frac{\kappa_Y}{\nu} = \frac{2\times\tau_\nu - 1}{2\times\tau_Y - 1} \quad (8)$$

The solution to the BGK evolution equation is usually acquired in two separate steps, i.e., the collision:

$$f_i(\mathbf{x} + \mathbf{e}_i\delta_t, t + \delta_t) = f(\mathbf{x}, t) - \frac{1}{\tau}\Big[f_i(\mathbf{x}, t) - f_i^{eq}(\mathbf{x}, t)\Big] \quad (9)$$

and the propagation

$$f_i(\mathbf{x} + \mathbf{e}_i\delta_t, t + \delta_t) = f(\mathbf{x}, t + \delta_t) \quad (10)$$

The most common BGK method employed in two-dimensional (2D) simulations discretizes the molecular velocities over nine directions (D2Q9 formalism). The components and weight factors are given as follows [33]:

$$e_i = \begin{cases} (0,\ 0) & i = 0 \\ (\cos((i-1)\pi/2), \sin((i-1)\pi/2)) & i = 1\sim4 \\ \sqrt{2}(\cos((i-1)\pi/2+4/\pi), \sin((i-1)\pi/2+4/\pi)) & i = 5\sim8 \end{cases}$$
$$\quad (11)$$

$$\omega_i = \begin{cases} 4/9 & i = 0 \\ 1/9 & i = 1 \sim 4 \\ 1/36 & i = 5 \sim 8 \end{cases} \quad (12)$$

In LBM simulation, both the grid size and time step are unity. So, the physical values need to be normalized and rescaled in the lattice space for simulation. The rule for the conversion is to keep a dimensionless number to be identical in both the lattice space and the physical system. The most common dimensionless numbers are the Reynolds number (Re) for flow, the Prandtl number (Pr) for heat transfer and the Schmidt number (Sc) for species transport. In the present study, the normalization of the source terms follows the procedure discussed in Refs. [17,37]. The numerical implementation in DL_MESO [32] has been validated on a constant-density, counterflow premixed propane flame. More details about the conversion method and validation results can be found in the supplementary material.

3. LBM simulation of gas-solid two-phase reacting flow

3.1. Char-combustion and alkali-release models

Well-established models for solid-char combustion and alkali release are combined with the LBM to simulate the combustion of a Zhundong coal pellet, previously studied experimentally [25].

During char combustion, oxygen diffuses to the solid surface to react with carbon to form CO and CO_2. Following [38], the reaction
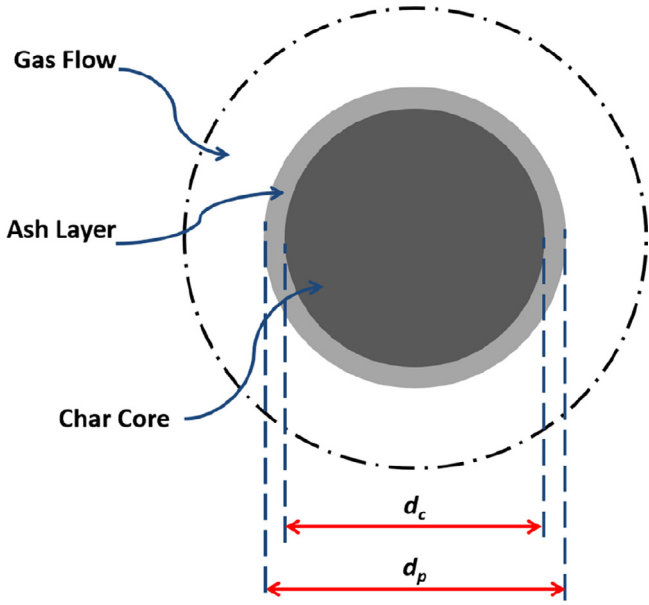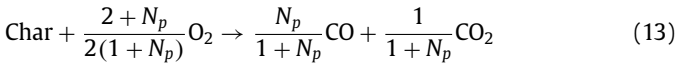
Fig. 1. Schematic diagram of the particle diameter d_p and the diameter d_c of the char core particle, excluding the ash layer.

rate is modeled with the char temperature and the CO/CO$_2$ mole ratio (N_p). Neglecting the effect of char gasification, the carbon reaction on the solid surface reads [38,39]:

$$\text{Char} + \frac{2+N_p}{2(1+N_p)}O_2 \rightarrow \frac{N_p}{1+N_p}CO + \frac{1}{1+N_p}CO_2 \qquad (13)$$

$$N_p = \frac{X_{CO}}{X_{CO_2}} = 3 \times 10^8 \exp\left(\frac{-60 \text{ kcal/mol}}{R \times T}\right) \qquad (14)$$

$$m_{comb} = A_s \times \frac{k_D}{k_{D_0}} \times C_{o,surface} \times 5.98 \times 10^4 \exp\left(\frac{-50.1 \text{ kJ/mol} \cdot K}{R \times T_{char}}\right) \qquad (15)$$

where X_j is the mole fraction (-) of species j; A_s is the reaction surface area (m^2) denoted by the burning rate m_{comb} (kg/s); $C_{o,surface}$ is the oxygen mass per unit area at the particle surface (kg/m^2); k_D is the oxygen diffusion coefficient (m^2/s); R is the universal gas constant (kJ/mol); T and T_{char} are the gas- and solid-phase temperatures (K), respectively. Since ash forming around the particle will inhibit the oxygen diffusion process, the ratio of k_D/k_{D0} was amended to incorporate the inhibition effect. The correction is expressed as, following [38,40]:

$$\frac{k_D}{k_{D_0}} = \frac{d_p T_0}{d_{p_0} T} \frac{(\text{Sh } \delta d_{c_0} + \theta^{2.5} d_{c_0}^2)}{(\text{Sh } \delta d_c + \theta^{2.5} d_c^2)} \qquad (16)$$

where δ is the ash thickness (m); Sh is the Sherwood number (–); θ is the porosity of ash (–), usually ranging from 0.15 to 0.21; d_p is the particle diameter (m) and d_c is the diameter (m) of the char core particle, excluding the ash layer, as shown in Fig. 1.

The carbon conversion ratio (–), C_{char}, is calculated from $m_{char,0}$, the initial char mass (kg), as follows:

$$C_{char} = \left(1 - \frac{m_{char}}{m_{char,0}}\right) \times 100\% \qquad (17)$$

In the simulation, C_{char} can be obtained from the ratio between the initial and current numbers of solid phase grid points. Then d_p and d_c can be determined by:

$$\rho_c = \frac{m_{char,0} + m_{ash,0}}{\frac{4\pi}{3}\left(\frac{d_{p,0}}{2}\right)^3} \qquad (18)$$

$$m_c = (m_{char,0} + m_{ash,0}) \times (1 - C_{char})$$

$$d_c = \left(\frac{3m_c}{4\pi \times \rho_c}\right)^{1/3} \times 2 \qquad (19)$$

$$d_p = \left(\frac{3 \times C_{char} \times m_{ash,0}}{4\pi \times \rho_{ash}} + \left(\frac{d_c}{2}\right)^3\right)^{1/3} \qquad (20)$$

$m_{ash,0}$ is the initial ash mass in the solid fuel particle (kg); m_c is the mass of the char core (kg); ρ_{ash} is the ash density (kg/m^3). The char and ash densities were set to be 1100 kg/m^3 and 900 kg/m^3, respectively. In addition, the Sherwood number for a sphere is defined as:

$$\text{Sh} = 2 + 0.6 \times \text{Re}^{1/2}\text{Sc}^{1/2} \qquad (21)$$

The sodium release rate calibrated from our previous experimental work [25] is used:

$$Na_{flux} = C_{Na} \times m_p \times 10^{6.118} \times \exp\left(\frac{-287.8 \text{ kJ/mol}}{R \times T}\right) \qquad (22)$$

where m_p is the particle mass (kg) and C_{Na} is the sodium mass fraction (–) in the char, with $C_{Na} = 0.287\%$ experimentally calibrated for Zhundong char. The sodium release rate Na_{flux} (kg/s) calculated by the above model is the mass flow rate of the sodium element released from the whole burning particle. So, the sodium mass source term in the gas phase around the char pellet is this release rate divided by the mass flow rate of the gas phase flowing through the pellet.

The CO generated from char combustion eventually burns in the gas phase in the presence of oxygen. A one-step CO combustion mechanism is introduced with a reaction-released heat of 83 kJ/mol [41]:

$$CO + 0.5O_2 \rightarrow CO_2 \quad k = 2.23 \times 10^{12}\exp\left(\frac{-1.7 \times 10^5 \text{ kJ/mol}}{R \times T}\right) \qquad (23)$$
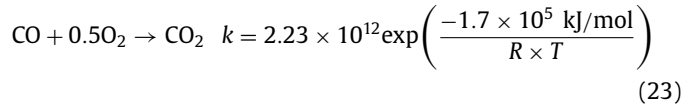
This CO$_2$ production rate k (kg/s) provides the heat release rate entering the balance equation for the temperature distribution function. At the solid phase surface, effects of thermal radiation Q_{rad} (kJ/s) and char combustion released heat Q_{comb} (kJ/s) are also considered[1] to compute the thermal budget of the solid phase,

$$Q_{rad} = \Delta^2 \varepsilon \sigma \left(T_{flow}^4 + T_{wall}^4 - 2T_{p,surface}^4\right)$$
$$Q_{comb} = Q_{heat} \times m_{comb} \qquad (24)$$
$$\Rightarrow Q = \frac{Q_{comb}}{\rho_{char}C_p} + \frac{Q_{rad}}{\Delta^3 \rho_{char}C_p}$$

where Δ is the resolution (m) of the LBM grid expressed in physical units; ε is the surface emissivity (–) and σ is the Stefan-Boltzmann constant (5.67×10^{-8} W m^{-2} K^{-4}); C_p is the heat capacity (kJ/(kg K)) of char. The emissivity ε and heat capacity C_p are corrected according to the mass fractions of the char and ash in the pellet and determined by a linear interpolation. The emissivity of char and ash is 0.85 and 0.5, respectively [42]. The C_p of both char and ash are a function of the pellet temperature, following the experimental data of Merrick et al. [43]:

$$C_p = \text{Char}\% \times C_{p,char} + \text{Ash}\% \times C_{p,ash} \qquad (25)$$

$$\varepsilon_p = \text{Char}\% \times \varepsilon_{p,char} + \text{Ash}\% \times \varepsilon_{p,ash} \qquad (26)$$

In practice, Q_{rad} is normalized by the char mass in the cell to advance in time the temperature distribution function.

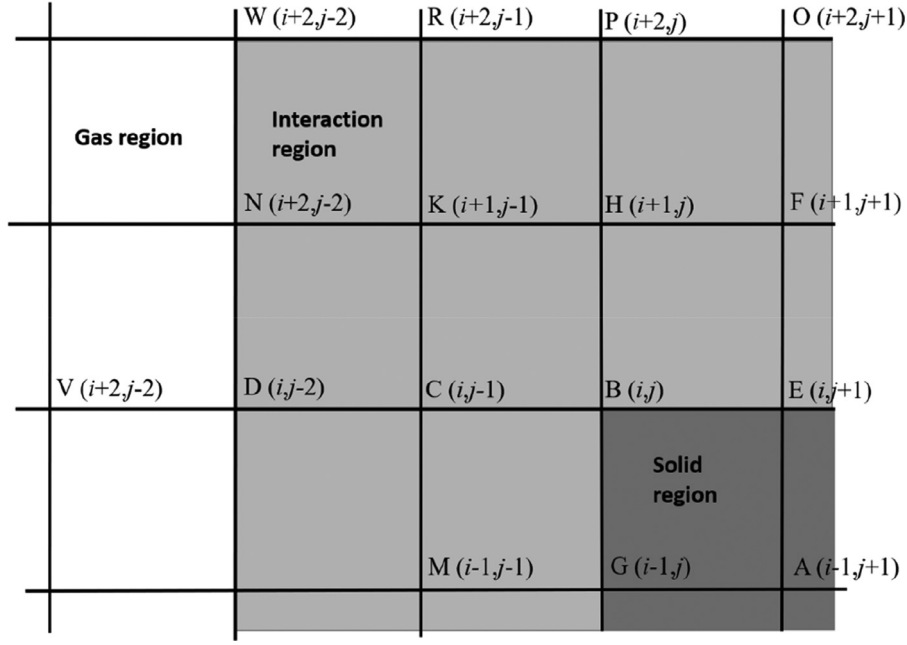[1] Notice that there is no heat source applied inside the solid phase.

Fig. 2. Schematic diagram of algorithms for solid-phase consumption during char combustion.

3.2. Algorithms for gas–solid two-phase interactions in combustion

Five types of grid points exist in the computational domain in addition to the boundaries, as illustrated in Fig. 2. They are organized as follows [44]: (a) grid points inside the solid phase, e.g., A in Fig. 2, on which only temperature conduction is calculated, and both species mass fractions and velocities are set to zero; (b) grid points on the solid-phase boundary (surface), e.g., B, E, and G in Fig. 2, on which the bounce back boundary condition was applied for flow velocity and species compositions, and the corresponding temperature source term (see Eq. (7)) is added according to the reaction; (c) grid points in the inner layer of the gas-solid interaction region, e.g., M, C, K, H, and F in Fig. 2, on which flow velocity and the scalars are solved, and the source terms are generated from both the solid-phase char combustion and the gas-phase CO reaction; (d) grid points in the outer layer of the gas-solid interaction region, e.g., D, N, W, R, P and O in Fig. 2. According to the buffer-zone interaction-layer approaches of immersed boundary theory [45–47], a two-layer interaction region has been used in the present study. For both the inner- and outer-layer interaction regions, the flow velocity and scalars are solved, and the source terms are generated from both the solid-phase char combustion and the gas-phase CO reaction; (e) grid points in the gas phase, e.g., V in Fig. 2, on which general LBM simulations were performed, and the source term was generated from CO combustion only.

The above five different types of grid points are distinguished in the simulation by constructing a phase function (f_{phase}). In Fig. 2, $f_{phase}(A)=4$, $f_{phase}(B)=3$, $f_{phase}(C)=2$, $f_{phase}(D)=1$ and $f_{phase}(V)=0$. For lattice points with the phase function '0', '1' or '2', the velocity, temperature, species compositions and density are solved; for grid points with the phase functions of '3' or '4', only temperature conduction is solved (notice that the same temperature distribution function is used for both phases, and only the sources are different). In addition, the difference of the heat diffusivity coefficient between the solid and gas phases was simulated by using different relaxation times for solid and gas grid points.

To model char consumption as combustion proceeds, a criterion based on the chemical reaction was set up for grid points on the solid phase boundary (e.g., B). For the convenience of distinguish-

ing between gas- and solid-phase grid points, a gas-solid mask f_{gs} is used. When the grid point is in the gas phase, $f_{gs}=0$. Otherwise $f_{gs}=1$. In the present study, the weight coefficients for the inner and outer interaction layers have been set to be 2/3 and 1/3, respectively, which means the inner and outer layers will receive 2/3 and 1/3 of the solid-phase combustion-generated heat and gaseous products, respectively, quantitatively as the mass and temperature source terms. In the simulation, the solid phase mass consumption m_{s_comb} (kg) of B-type grid points is determined by the reaction rate on the 24 surrounding grid points (in Fig. 2, D, C, N, K, H, W, R and P account for 1/4 of the total sampling region for B):

$$m_{s\_comb,t+dt} = m_{s\_comb,t} + \sum m_{comb} \times (1-f_{gs}) \times \frac{f_{phase}}{3} dt \quad (27)$$

where Σ denotes the summation of the contribution from the adjacent grid points around the local one; dt is the actual LBM time step (s).

The phase change is simulated by monitoring m_{s_comb}, the cumulated mass consumed on the solid lattice points. When m_{s_comb} exceeds 1/8 of the solid-phase mass over a lattice cell (each lattice point contributes 1/8), the phase function of the solid-gas boundary point (e.g., B in Fig. 2) is changed to that of the gas phase. The velocity and scalars are then approximated from the adjacent grid points (for B in Fig. 1, information from K, E, P, C, F and H shall be used). The species mass fractions are obtained by averaging and the temperature by energy conservation. To secure mass conservation, the burnt solid-phase mass is added to the total mass of the gas phase, and the reference gas density is recomputed. This numerical procedure may be summarized as (N_{gas} denotes the number of gas grid point):

$$\text{when } m_{s\_comb,t} > \frac{\Delta^3 \rho_{char}}{8}$$

$$\Rightarrow \begin{cases} f_{phase} = 1 \quad f_{gs} = 0 \\ Y = \frac{\sum Y_{gas} \times (1-f_{gs})}{N_{gas}} \quad T = T_{char} + \frac{Q_{heat} \times dm_{s\_comb}}{C_{p,char}\rho_{char}} \end{cases} \quad (28)$$

outlet, zero gradient

3 cm

4.5 cm

left, periodic

right, periodic
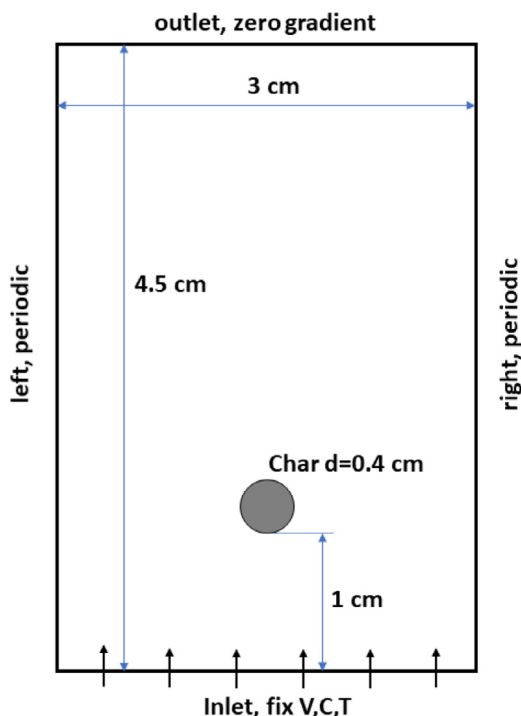
Char d=0.4 cm

1 cm

Inlet, fix V,C,T

Fig. 3. Simulation domain and boundary conditions.

3.3. Single char pellet combustion

In the experiment reported in [25], a 4-mm Zhundong coal pellet with an initial mass of 50 mg is suspended 1 cm above a laminar, fuel-lean (equivalence ratio: 0.8) methane flame. The diameter of the burner is 3 cm [48]. The composition of the gas flowing through the pellet is estimated from CHEMKIN calculations, which is 3.9% O_2, 7.6% CO_2, 15.4% H_2 and 72.8% N_2 (mass fractions) when the flow velocity is 0.15 m/s. The flame temperature is 1892 K, and the gas temperature is about 1600 K at the pellet location because of heat loss [25]. The coal pellet undergoes devolatilization, char burnout and ash cooking. The data for the char burnout stage was specifically extracted for the present work. The char burning started 50 s after ignition [27]. The initial mass and diameter of the char pellet are 35 mg and 4 mm, respectively. The swelling effect is neglected [42, 49]. During the whole course of the char burning, the temperature varies from 1600 K to 1760 K, and the flow Reynolds number based on the char pellet (0.004 m) and flow velocity (0.15 m/s) is 3.84.

The computational domain is 4.5 cm in height and 3 cm in width (Fig. 3). Following the conclusion of the grid independence study, the detail of which can be found in the supplemental material, a 427×285 grid is used. The bottom boundary is the inlet of the domain with fixed values of velocities and scalars. The top boundary is the outlet with zero normal gradients. The left and right boundaries are periodic (no thermal expansion included in the modeling). The inlet velocity is 0.15 m/s, and the inlet temperature is 1600 K. At the solid surface, the bounce back boundary condition is set for the flow and species mass fractions. To match physical flow properties, the relaxation time in the BGK model is set to 0.989. Both Pr and Sc are assumed to be unity.

The instantaneous simulation results of the shrinking char pellet, velocity and scalars at $C_{char} = 60\%$ are shown in Fig. 4(b)-(h). The image of the initial char pellet is shown in (a) for comparison.

As the combustion progresses, the mass of the char pellet is continuously consumed and the pellet size shrinks [compare

Fig. 4(a) with (b)]. Since oxygen is fed from the bottom of the pellet, the bottom surface of the char pellet is consumed faster than the top, making the char particle non-spherical. As expected, a wake develops downstream of the char pellet.

CO combustion increases gas temperature around the pellet. The heat capacity of the char being much higher than the gas one, the solid temperature stays below the gas temperature. The temperature distribution inside the solid particle stays almost uniform, which is consistent with the low Biot number estimated from the experimental study [25,27].

The oxygen reaching the solid surface reacts with char, generating CO and CO_2, so the O_2 mass fraction decreases around the pellet while the CO and CO_2 mass fractions increase. The generated CO further reacts with O_2 in the gas phase, thereby its mass fraction decreasing sharply.

Sodium vapor is released from the burning char pellet without further accounting for gas phase alkali reactions. Accordingly, the sodium concentration decreases as the sodium vapor travels away from the char pellet.

Comparisons against measurements of the char-particle mass and temperature evolutions are shown in Fig. 5, confirming the validity of the proposed approach. Because of the ash inhibition effect, the slope of the carbon conversion decreases with time. This phenomenon is well captured by the simulation. During the intermediate stage, however, the simulation slightly underpredicts the carbon burnout. This is attributed to ash inhibition over limiting the char burning because of the fixed value of θ used in Eq. (21). Indeed, the porosity of the ash should start at a lower value and then gradually increase towards $\theta = 0.2$, to match the carbon conversion measurement in the final stage. Instead of looking for an ad-hoc $\theta(t)$ response, it is discussed in a subsequent section how the internal char pellet topology can be included in the simulation.

Overall, the temperature result is consistent with the experimental one. At the initial stage the simulation underpredicts the char-particle temperature, but at the final stage overpredicts it. The difference at the initial stage is mainly attributed to the measurement itself. The volatile combustion, prior to the char combustion stage, heats the char pellet by flame radiation. However, this radiative effect of volatile burning was not considered in the simulation. The difference at the final stage is attributed to the evolution of the heat capacity and surface emission of the pellet, which are initially determined by carbon and later by ash. Even though a linear fitting was adopted in the simulation for the two parameters, it is still not accurate enough to reproduce the change of physical characteristics of the pellet, featuring a shrinking char core imbedded in a thickening ash layer.

The elemental sodium flux at 1 cm above the char pellet is collected as in the experiment. The elemental sodium is defined summing over all sodium species. The radial distributions of the elemental sodium concentration at 1 cm above the pellet are also shown in Fig. 6, for three different times when the carbon conversion ratio is 30%, 60% and 90%, respectively.

Considering the complexity of the processes at play, the predicted sodium fluxes are in quite good agreement with the LIBS measurements. Because of the lower temperature predictions, the sodium mass fractions at early times are lower than the experimental data. Similarly, the overprediction of temperature at the final stage leads to an overprediction of sodium release, to which should be added the uncertainty in the experimental determination of the sodium flux from the LIBS measurement (which, for instance, neglects the effect of the shrinking pellet on the gas flow). Moreover, the measured velocity distribution at the initial stage was used to calculate the integral of the sodium fluxes in the char burnout stages. In fact, the velocity distribution evolves because of the shrinking of the pellet. So, the sodium flux is expected to be larger than the value measured by LIBS.
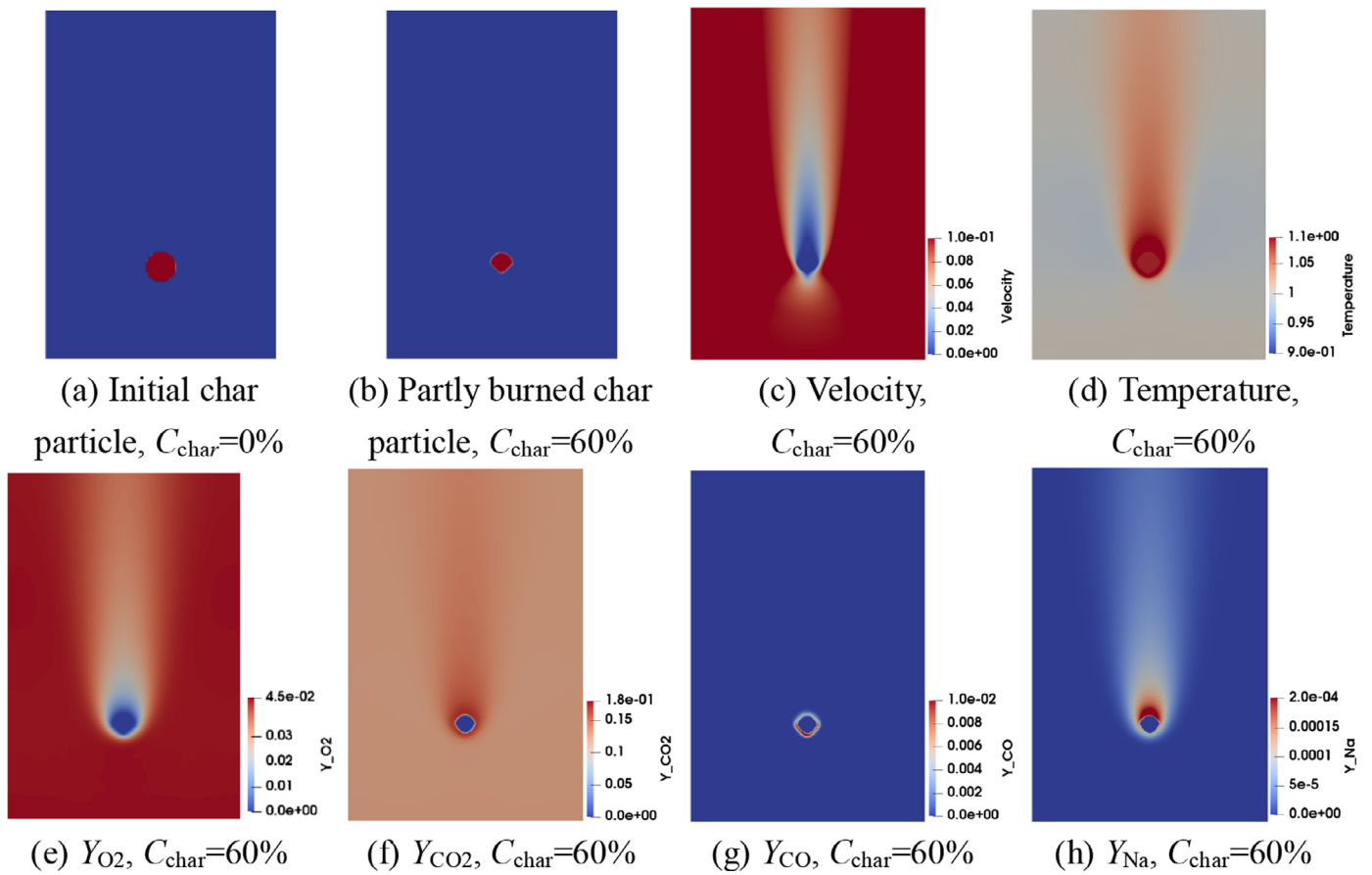
(a) Initial char particle, $C_{char}=0\%$

(b) Partly burned char particle, $C_{char}=60\%$

(c) Velocity, $C_{char}=60\%$

(d) Temperature, $C_{char}=60\%$

(e) Y_{O2}, $C_{char}=60\%$

(f) Y_{CO2}, $C_{char}=60\%$

(g) Y_{CO}, $C_{char}=60\%$

(h) Y_{Na}, $C_{char}=60\%$

Fig. 4. Instantaneous LBM simulation results of char-pellet combustion ($C_{char} = 60\%$).

(a) Carbon conversion ratio

(b) Solid-phase temperature
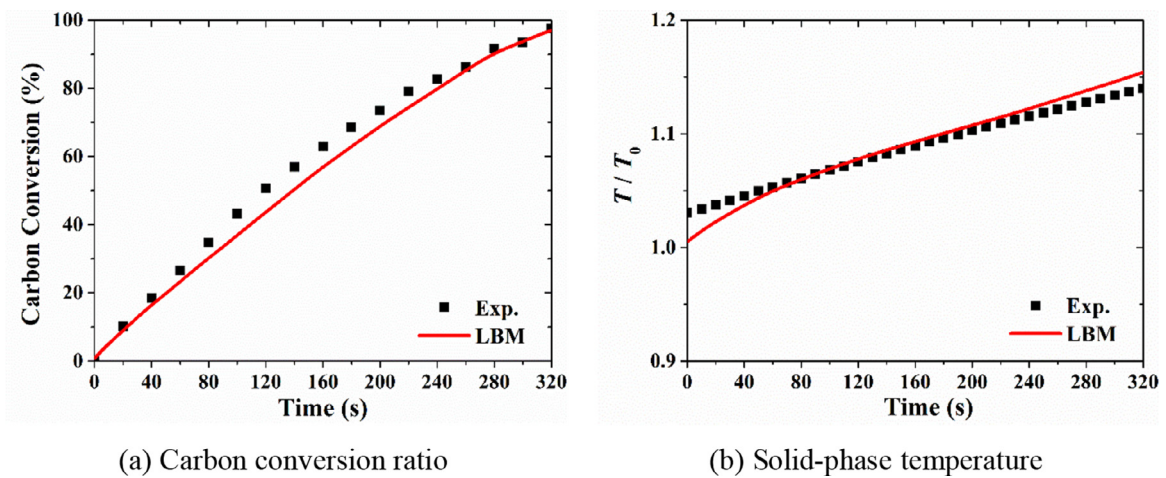
Fig. 5. Comparison between LBM simulation and experimental results on particle mass and temperature.
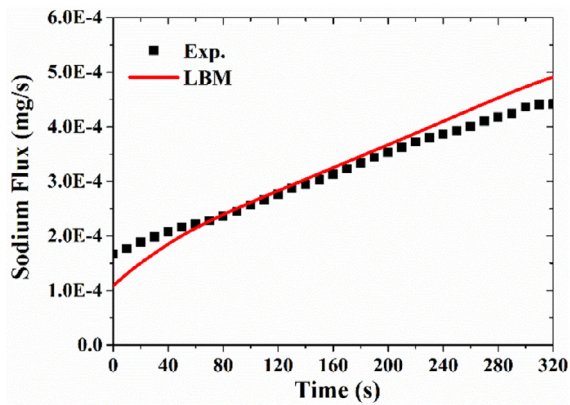
The prediction of the radial distribution of the elemental sodium concentration shows a similar trend to that of the sodium flux. It is lower than the experimental profile at the initial stage, and becomes higher at the final stage of the char combustion, still with a very encouraging overall agreement. The simulation underpredicts the radial span of sodium diffusion. All the simulation results at the radial distance of 0.009 m ($r/L = 2.25$) from the centerline are lower than the measurements. First, the released sodium includes the sodium element from a variety of sodium species, which may undergo differential diffusion. But in the simulation, the Schmidt number was set to unity. Second, the

presence of ash is likely to introduce fluctuations in the sodium release and thereby variability in the gas phase distributions, a phenomenon which is neglected in the simulation.

3.4. Porous char combustion and sodium release

The developed LBM simulation framework is now used to explore porous-char combustion and sodium release from porous char. The porous char structure is taken from Minkina et al. [50] on pyrolysis of a subbituminous coal particle under 1073 K. The computational configuration is shown in Fig. 7. The physical

(a) Elemental sodium flux
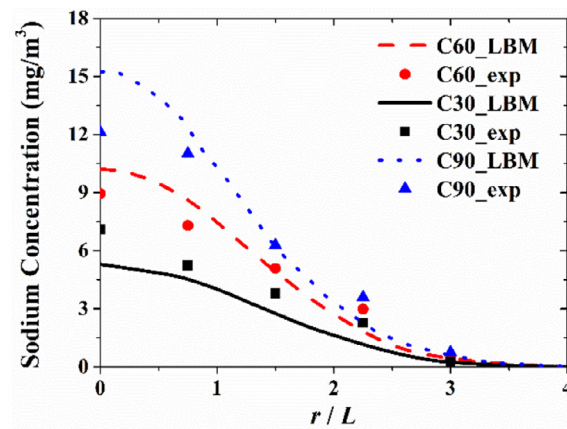
(b) Radial distribution of elemental sodium

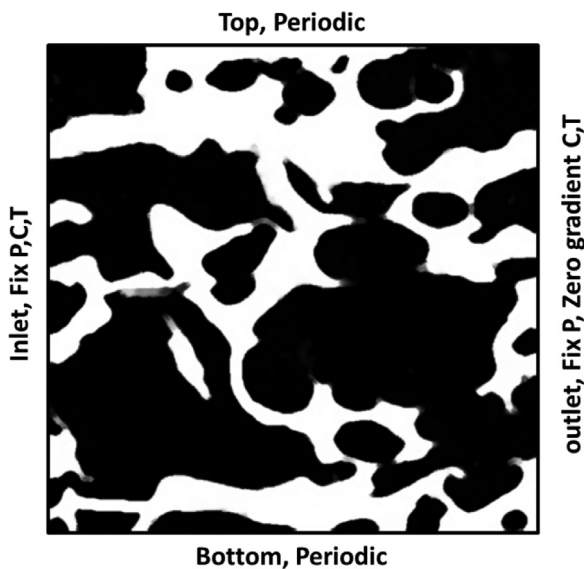Fig. 6. Comparison of sodium profiles between simulation and measurement.

Fig. 7. Porous char structure and boundary conditions of LB simulation.

size of the porous-char image is $500 \times 500 \mu m$. The selected microstructure features pore blockage, flow channel bifurcation and closed pores inside the char, with an overall porosity of 21.5%.

The objective is to model the combustion of a char particle transported by a flow and entering a high temperature zone. Imposing a 2/3 pressure drop between the left and right boundaries of the two-dimensional lattice, a flow develops through the char with a Reynolds number of the order of 1.2, a value which is representative of flow regimes usually observed in such porous media. Initially, the porous char is filled with cold air (300 K). The hot air entering the simulated domain at a temperature of 1600 K contains 23.3% oxygen and 76.7% nitrogen in mass fractions. After checking the grid independence, a 300×300 lattice grid is used. A zero-gradient boundary condition is used for all the scalars at the outlet. The top and bottom boundaries of the domain are set as periodic. As above, the bounce back boundary for flow velocity and species mass fractions is applied at the solid surface, and heat conduction is solved inside the solid phase.

The characteristic parameters of Zhundong char are applied as they are very close to those of the subbituminous coal sample used to build the porous structure for the simulation [50]. The

density, reaction parameters and sodium proportion are therefore those of Section 4.3, which have been used to validate the LBM methodology against experimental measurements. In the present simulation, reactions due to CO in the gas phase and char on the solid phase surface are both considered. Because the amount of ash generated in this porous structure is expected to be small, the ash inhibition effect on oxygen diffusion is also neglected.

Figure 8 shows the results observed at the time when 20% of the carbon conversion is reached. The flow proceeds from left to right and, because of the higher temperature carried by the flow, the left side of the porous char structure is firstly consumed. Two main flow channels are established. As these channels become narrowed or bended, the gas flow accelerates or changes its direction, with significant acceleration in the narrower zones. It can be observed that CO generated at the char surface will burn at the front side of the domain facing the incoming flow, causing local high temperature that further heats the char structure.

The evolution of the porous structure and velocity distribution during the porous char combustion processes are shown in Fig. 9 when the carbon conversion ratio is 0%, 20%, 40%, 60%, 80% and 100%. Closed pore spaces are opened and narrow flow paths are expanded during char combustion, followed by an increase of the porosity. This increase in porosity stimulates the overall burning rate of char, and the destruction of internal pores releases the gas phase components that were previously stored in the closed pores, such as the alkali metal vapor.

Figure 10 shows that a significant proportion of the oxygen entering the domain is consumed upfront of the char by combustion both in the gas phase and on the solid surface. The remaining oxygen diffuses through flow channels to react at the solid-char surface to produce carbon monoxide and carbon dioxide. These species are then transported into the porous medium. Due to the complicated flow paths in the porous structure and the smaller gas flow rate, the generated CO and CO_2 tend to accumulate at the reaction front, with also a certain ability to diffuse upstream. Some parts of CO will also reacted with the coming O_2 and forming CO_2. At early times, CO and CO_2 presented deep inside the porous structure are due to flow transport and molecular diffusion, since there is a lack of oxygen there.

Interestingly, the distribution characteristics of sodium vapor released into the gas phase differ from those of the combustion products (Fig. 10). The regions with high combustion-product concentrations mainly feature the highest momentum levels, while the regions with a high concentration of sodium are mainly those with a weak flow velocity. Although sodium vapor is released from
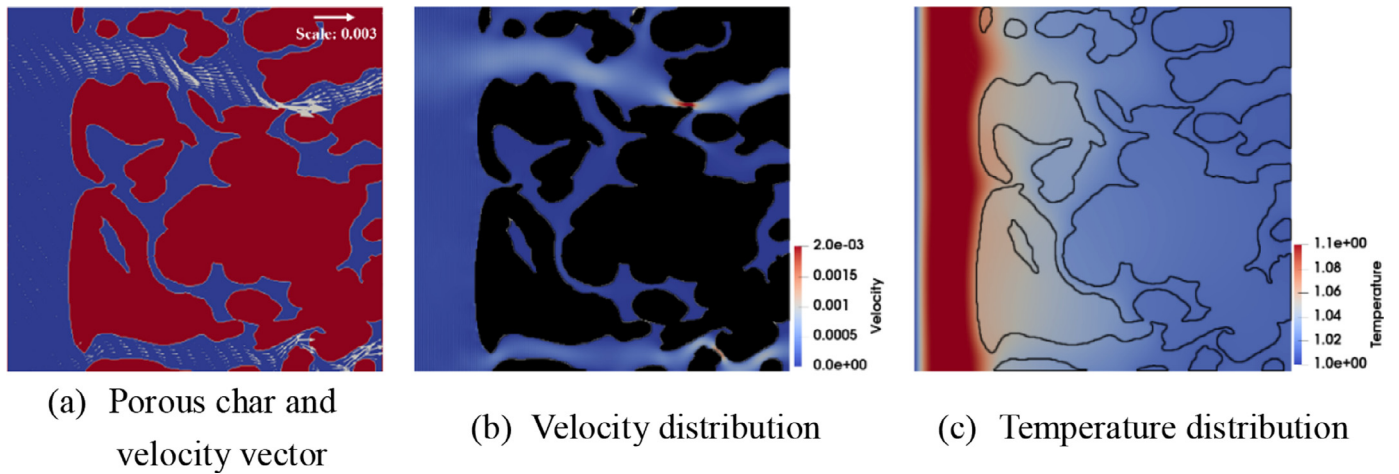
(a) Porous char and velocity vector

(b) Velocity distribution

(c) Temperature distribution

Fig. 8. Instantaneous velocity and temperature distributions in porous char at $C_{char} = 20\%$.

(a) C_{char}==0%

(b) C_{char}==20%

(c) C_{char}==40%

(d) C_{char}==60%

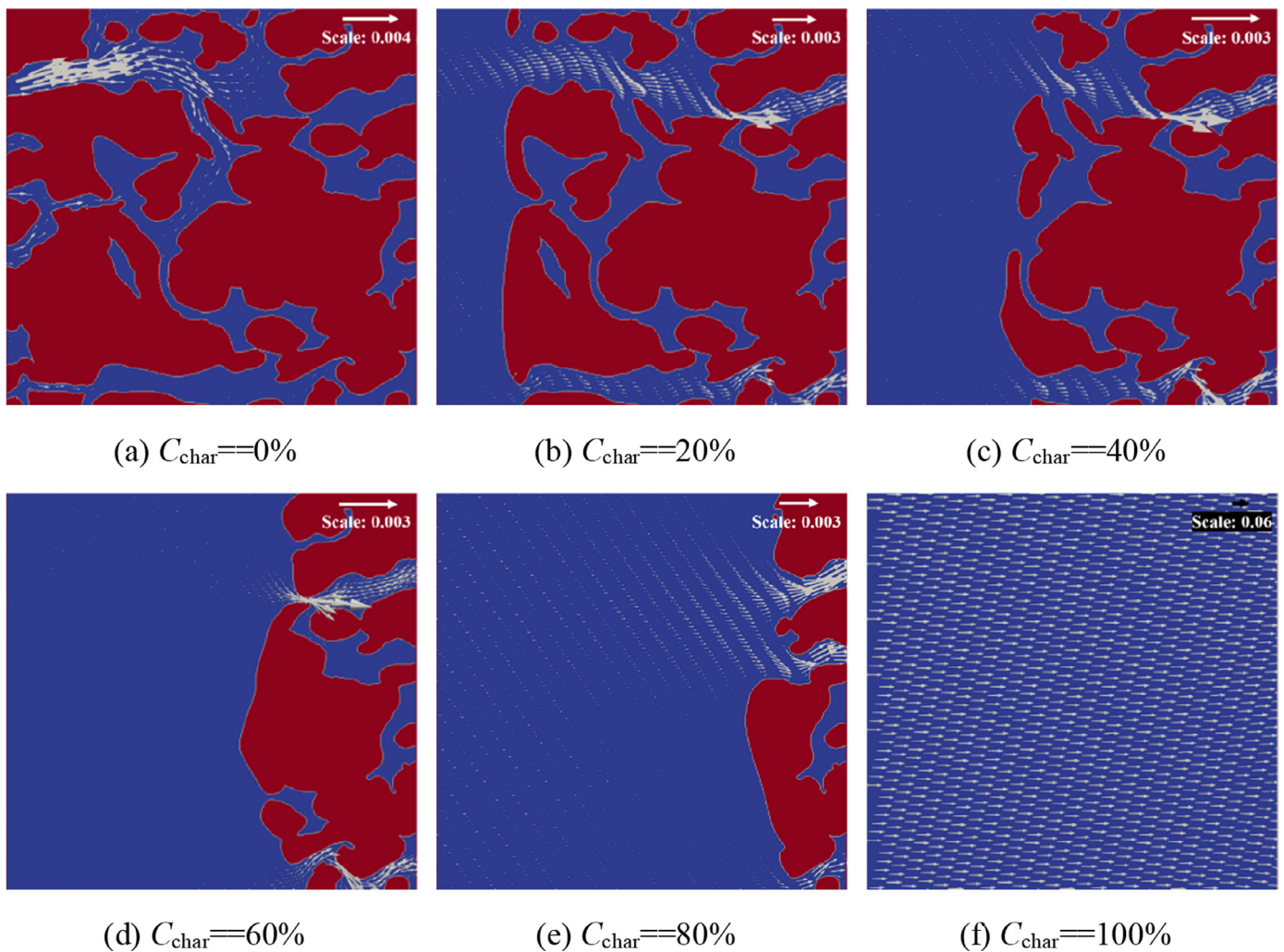(e) C_{char}==80%

(f) C_{char}==100%

Fig. 9. Evolution of porous structure and flow field during porous char combustion.

the solid phase by heating, there is not that much of sodium at the flame locations. Indeed, because of the large differences in transport properties between the gas and solid phases, once released, the sodium vapor rapidly diffuses inside the microchannels, while the solid char needs to be heated for its consumption to propagate. On the other hand, in retarded flow channels and closed pores, where flow transport is limited, the continuous accumulation of sodium vapor released makes its concentration higher.

It should be pointed out that LBM simulation has also been performed for the burning of a Zhundong coal char particle with a lower overall porosity 11.1% (results not shown). The porous structure was taken from in-house SEM (Scanning Electron
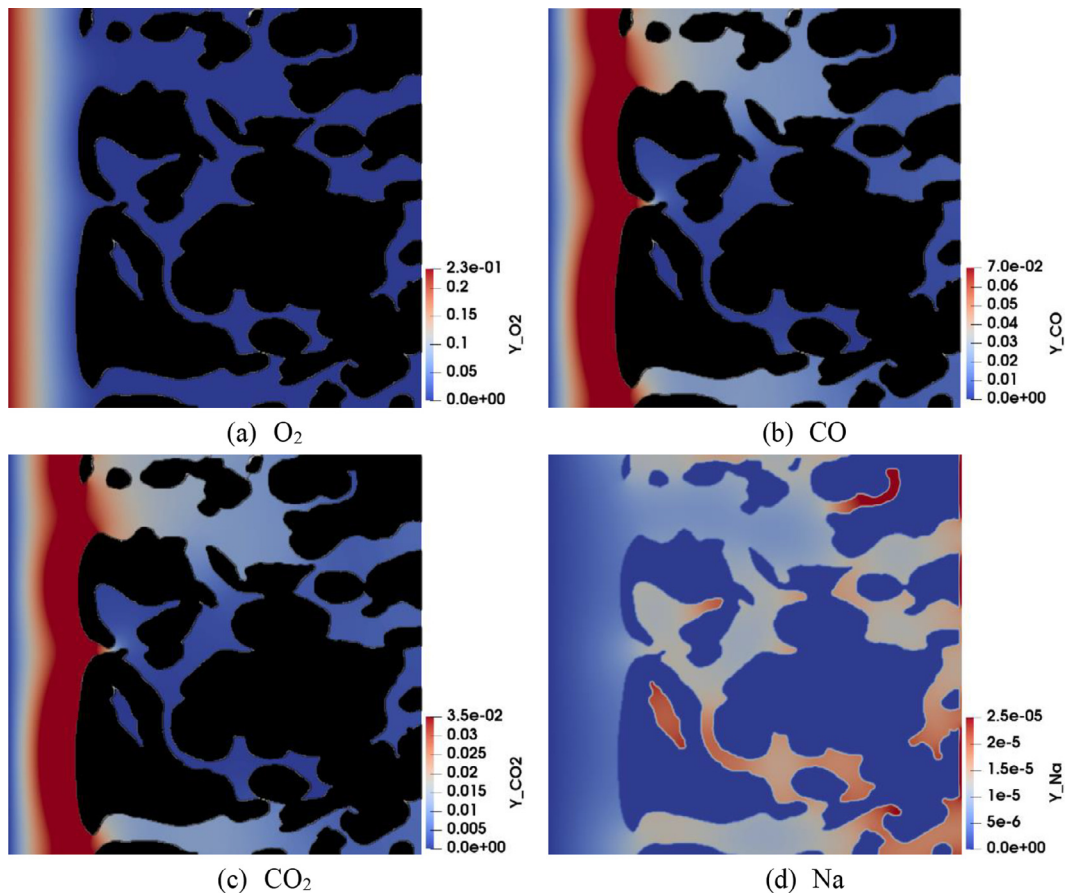
(a) O₂

(b) CO

(c) CO₂

(d) Na

Fig. 10. Species distributions inside porous char at $C_{char} = 20\%$.

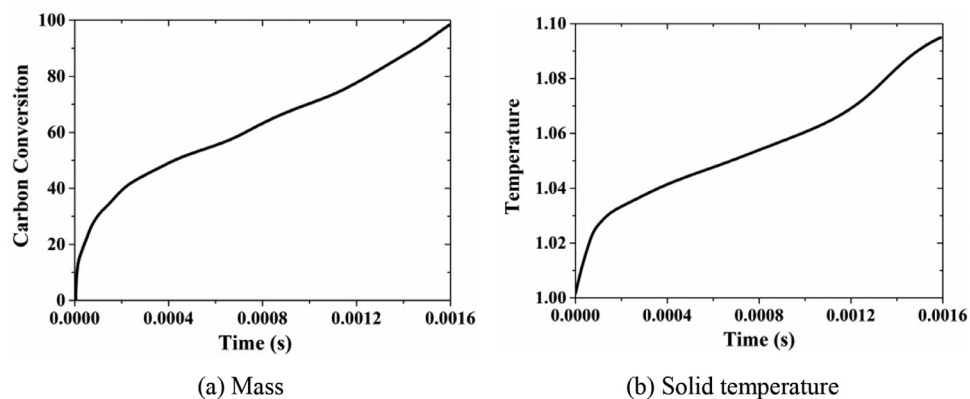
(a) Mass

(b) Solid temperature

Fig. 11. Averaged carbon conversion ratio and solid phase temperature during porous char combustion.

Microscope) images. Except that the time scale for the Zhundong coal char particle to complete burning is longer due to a lower porosity, we observed an identical trend of the distribution characteristics of combustion products and sodium vapor in the porous structure.

The time evolution of the average over the computational domain of the carbon conversion and solid-phase temperature is shown in Fig. 11. As the combustion progresses, the slope of the carbon conversion ratio slightly decreases after a first increase, and then increases again. This sequence is explained by the fact that the char close to the left boundary, thus directly encountering the incoming oxygen, burns very quickly; as the combustion progresses, the flame front of the char reaction is gradually moving away from the left boundary, and the accumulation of the combustion products and CO combustion in the gas phase weakens the diffusion of oxygen to the reaction front, thereby decreasing the char burning rate. As the combustion of char further continues, narrow flow channels expand, oxygen diffusion proceeds and the increased reaction specific surface area favors char combustion again. At the initial stage of the combustion, the solid phase temperature starts to rise due to the heating by both char combustion on the solid surface and CO combustion in the gas phase. As the reaction proceeds, the reaction front shifts towards the right, the unreacted proportion of the solid phase decreases, making the average temperature increase. At the final stage of the char combustion, the solid phase reaction rate is enhanced by the accelerated gas diffusion and the reduced reaction area, so a further increase of the average temperature is observed.

4. Conclusions

Char combustion and alkali metal (sodium) release in a porous-char particle were investigated using a lattice Boltzmann method. The standard LBM flow formalism is modified to account for a solid fuel phase, including gaseous and surface chemical reactions. Single-step global kinetics are used and the decomposition of ash was not considered, but the inhibition of ash on oxygen diffusion is included.

The LBM simulation results were first validated against previous char combustion and sodium release measurements. The pellet mass, particle temperature and sodium release are in quite good agreement with the experimental data, demonstrating the prediction capabilities of the proposed approach.

The combustion of an actual sub-bituminous porous char particle is then addressed, simulating the flow dynamics inside the particle. The production and diffusion of CO and CO_2 inside the porous char structure follows the internal flow direction; due to CO combustion in the gas phase and char burning on the solid surface, most oxygen is consumed at the reaction front bordering the particle, thus limiting the diffusion of O_2 inside the porous medium; because of the different heat and mass transfer and chemical time scales at play, the distribution of the volatile products, such as sodium vapor, differs from that of the combustion products CO/CO_2.

Declaration of Competing Interest

We declare that we have no financial and personal relationships with other people or organizations that can inappropriately influence our work. There is no professional or other personal interest of any nature or kind in any product, service and/or company that could be construed as influencing the position presented in, or the review of, the manuscript entitled, "Simulation of char-pellet combustion and sodium release inside porous char using lattice Boltzmann method".

Acknowledgments

Supplementary materials

Supplementary material associated with this article can be found, in the online version, at doi:10.1016/j.combustflame.2019.10.005.

References

[1] H. Chen, S. Chen, W.H. Matthaeus, Recovery of the Navier-Stokes equations using a lattice-gas Boltzmann method, Phys. Rev. A 45 (1992) R5339.
[2] X. He, L.-S. Luo, Theory of the lattice Boltzmann method: from the Boltzmann equation to the lattice Boltzmann equation, Phys. Rev. E 56 (1997) 6811.
[3] S. Chen, G.D. Doolen, Lattice Boltzmann method for fluid flows, Annu. Rev. Fluid Mech. 30 (1998) 329–364.
[4] Q. Li, K.H. Luo, Q. Kang, Y. He, Q. Chen, Q. Liu, Lattice Boltzmann methods for multiphase flow and phase-change heat transfer, Prog. Energy Combust. Sci. 52 (2016) 62–105.
[5] X. He, G.D. Doolen, Thermodynamic foundations of kinetic theory and lattice Boltzmann models for multiphase flows, J. Stat. Phys. 107 (2002) 309–328.
[6] J. Wang, L. Chen, Q. Kang, S.S. Rahman, The lattice Boltzmann method for isothermal micro-gaseous flow and its application in shale gas flow: a review, Int. J. Heat Mass Transf. 95 (2016) 94–108.
[7] Y. Yan, Y. Zu, Numerical simulation of heat transfer and fluid flow past a rotating isothermal cylinder–a LBM approach, Int. J. Heat Mass Transf. 51 (2008) 2519–2536.
[8] M. Sheikholeslami, H. Ashorynejad, P. Rana, Lattice Boltzmann simulation of nanofluid heat transfer enhancement and entropy generation, J. Mol. Liq. 214 (2016) 86–95.
[9] M. Sheikholeslami, M. Gorji-Bandpy, G. Domairry, Free convection of nanofluid filled enclosure using lattice Boltzmann method (LBM), Appl. Math. Mech. 34 (2013) 833–846.
[10] H. Liu, Q. Kang, C.R. Leonardi, S. Schmieschek, A. Narváez, B.D. Jones, J.R. Williams, A.J. Valocchi, J. Harting, Multiphase lattice Boltzmann simulations for porous media applications, Comput. Geosci. 20 (2016) 777–805.
[11] Z. Guo, T. Zhao, Lattice Boltzmann model for incompressible flows through porous media, Phys. Rev. E 66 (2002) 036304.
[12] Y. Liu, R. He, Modeling of the pore structure evolution in porous char particles during combustion, Combust. Sci. Technol. 188 (2016) 207–232.
[13] J. Buckles, R. Hazlett, S. Chen, K. Eggert, D. Grunau, W. Soll, Flow through porous media using lattice Boltzmann method, Los Alamos Sci. 22 (1994) 112–121.
[14] Q. Kang, P.C. Lichtner, D.R. Janecky, Lattice Boltzmann method for reacting flows in porous media, Adv. Appl. Math. Mech. 2 (2010) 545–563.
[15] L. Chen, Q. Kang, B. Carey, W.Q. Tao, Pore-scale study of diffusion–reaction processes involving dissolution and precipitation using the lattice Boltzmann method, Int. J. Heat Mass Transf. 75 (2014) 483–496.
[16] J. Gao, H. Xing, L. Turner, K. Steel, M. Sedek, S.D. Golding, V. Rudolph, Pore-scale numerical investigation on chemical stimulation in coal and permeability enhancement for coal seam gas production, Transp. Porous Media 116 (2017) 335–351.
[17] K. Yamamoto, N. Takada, M. Misawa, Combustion simulation with Lattice Boltzmann method in a three-dimensional porous structure, Proc. Combust. Inst. 30 (2005) 1509–1515.
[18] C. Lin, K.H. Luo, Mesoscopic simulation of nonequilibrium detonation with discrete Boltzmann method, Combust. Flame 198 (2018) 356–362.
[19] Y. Feng, M. Tayyab, P. Boivin, A Lattice-Boltzmann model for low-Mach reactive flows, Combust. Flame 196 (2018) 249–254.
[20] C. Lin, K.H. Luo, L. Fei, S. Succi, A multi-component discrete Boltzmann model for nonequilibrium reactive flows, Sci. Rep. 7 (2017) 14580.
[21] C. Lin, K.H. Luo, Discrete Boltzmann modeling of unsteady reactive flows with nonequilibrium effects, Phys. Rev. E 99 (2019) 012142.
[22] S.A. Hosseini, N. Darabiha, D. Thévenin, Mass-conserving advection–diffusion Lattice Boltzmann model for multi-species reacting flows, Physica A 499 (2018) 40–57.
[23] Y. Niu, H. Tan, Hui, ash-related issues during biomass combustion: alkali-induced slagging, silicate melt-induced slagging (ash fusion), agglomeration, corrosion, ash utilization, and related countermeasures, Prog. Energy Combust. Sci. 52 (2016) 1–61.
[24] Y. Niu, H. Tan, L. Ma, M. Pourkashanian, Z. Liu, Y. Liu, X. Wang, H. Liu, T. Xu, Slagging characteristics on the superheaters of a 12 MW biomass-fired boiler, Energy Fuels 24 (2010) 5222–5227.
[25] Y. Liu, Y. He, Z. Wang, K. Wan, J. Xia, J. Liu, K. Cen, Multi-point LIBS measurement and kinetics modeling of sodium release from a burning Zhundong coal particle, Combust. Flame 189 (2018) 77–86.
[26] Y. He, J. Zhu, B. Li, Z. Wang, Z. Li, M. Aldén, K. Cen, In-situ measurement of sodium and potassium release during oxy-fuel combustion of lignite using laser-induced breakdown spectroscopy: effects of O_2 and CO_2 concentration, Energy Fuels 27 (2013) 1123–1130.
[27] Z. Wang, Y. Liu, R. Whiddon, K. Wan, Y. He, J. Xia, K. Cen, Measurement of atomic sodium release during pyrolysis and combustion of sodium-enriched Zhundong coal pellet, Combust. Flame 176 (2017) 429–438.
[28] P. Van Eyk, P. Ashman, Z. Alwahabi, G. Nathan, Quantitative measurement of atomic sodium in the plume of a single burning coal particle, Combust. Flame 155 (2008) 529–537.
[29] K. Wan, J. Xia, L. Vervisch, Y. Liu, Z. Wang, K. Cen, Modelling alkali metal emissions in large-eddy simulation of a preheated pulverised-coal turbulent jet flame using tabulated chemistry, Combust. Theory Model. 22 (2018) 203–236.
[30] K. Wan, L. Vervisch, J. Xia, P. Domingo, Z. Wang, Y. Liu, K. Cen, Alkali metal emissions in an early-stage pulverized-coal flame: DNS analysis of reacting layers and chemistry tabulation, Proc. Combust. Inst. 37 (2019) 2791–2799.
[31] P. Glarborg, P. Marshall, Mechanism and modeling of the formation of gaseous alkali sulfates, Combust. Flame 141 (2005) 22–39.
[32] M.A. Seaton, R.L. Anderson, S. Metz, W. Smith, DL_MESO: highly scalable mesoscale simulations, Mol. Simul. 39 (2013) 796–821.
[33] Z. Guo, C. Zheng, B. Shi, Discrete lattice effects on the forcing term in the lattice Boltzmann method, Phys. Rev. E 65 (2002) 046308.
[34] L. Fei, K.H. Luo, Cascaded lattice Boltzmann method for thermal flows on standard lattices, Int. J. Thermal Sci. 132 (2018) 368–377.
[35] L. Fei, K.H. Luo, Q. Li, Three-dimensional cascaded lattice Boltzmann method: improved implementation and consistent forcing scheme, Phys. Rev. E 97 (2018) 053309.
[36] C. Lin, K.H. Luo, MRT discrete Boltzmann method for compressible exothermic reactive flows, Comput. Fluids 166 (2018) 176–183.
[37] K. Yamamoto, X. He, G.D. Doolen, Simulation of combustion field with lattice Boltzmann method, J. Stat. Phys. 107 (2002) 367–383.
[38] R. Hurt, J.-K. Sun, M. Lunden, A kinetic model of carbon burnout in pulverized coal combustion, Combust 113 (1998) 181–197.
[39] M. Cloke, T. Wu, R. Barranco, E. Lester, Char characterisation and its application in a coal burnout model, Fuel 82 (2003) 1989–2000.
[40] S. Niksa, G.-s. Liu, R.H. Hurt, Coal conversion submodels for design applications

at elevated pressures. Part I. Devolatilization and char oxidation, Prog. Energy Combust. Sci. 29 (2003) 425–477.

[41] C.-L. Yeh, Numerical analysis of the combustion and fluid flow in a carbon monoxide boiler, Int. J. Heat Mass Transf. 59 (2013) 172–190.

[42] K. Wan, Z. Wang, Y. He, J. Xia, Z. Zhou, J. Zhou, K. Cen, Experimental and modeling study of pyrolysis of coal, biomass and blended coal–biomass particles, Fuel 139 (2015) 356–364.

[43] D. Merrick, Mathematical models of the thermal decomposition of coal: 2. Specific heats and heats of reaction, Fuel 62 (1983) 540–546.

[44] T. Min, Y. Gao, L. Chen, Q. Kang, W.Q. Tao, Changes in porosity, permeability and surface area during rock dissolution: effects of mineralogical heterogeneity, Int. J. Heat Mass Transf. 103 (2016) 900–913.

[45] K.S. Kedia, C. Safta, J. Ray, H.N. Najm, A.F. Ghoniem, A second-order coupled immersed boundary-SAMR construction for chemically reacting flow over a heat-conducting Cartesian grid-conforming solid, J. Comput. Phys. 272 (2014) 408–428.

[46] I. Borazjani, L. Ge, F. Sotiropoulos, Curvilinear immersed boundary method for simulating fluid structure interaction with complex 3D rigid bodies, J. Comput. Phys. 227 (2008) 7587–7620.

[47] A. Calderer, S. Kang, F. Sotiropoulos, Level set immersed boundary method for coupled simulation of air/water interaction with complex floating structures, J. Comput. Phys. 277 (2014) 201–227.

[48] Y. He, Z. Wang, W. Weng, Y. Zhu, J. Zhou, K. Cen, Effects of CO content on laminar burning velocity of typical syngas by heat flux method and kinetic modeling, Int. J. Hydrog. Energy 39 (2014) 9534–9544.

[49] Z. Wang, K. Wan, J. Xia, Y. He, Y. Liu, J. Liu, Pyrolysis characteristics of coal, biomass, and coal–biomass blends under high heating rate conditions: effects of particle diameter, fuel type, and mixing conditions, Energy Fuels 29 (2015) 5036–5046.

[50] M. Minkina, F. Oliveira, V. Zymla, Coal lump devolatilization and the resulting char structure and properties, Fuel Process. Technol. 91 (2010) 476–485.